DOI: 10.1002/chem.200701565

Modelling Amphetamine/Receptor Interactions: A Gas-Phase Study of Complexes Formed between Amphetamine and Some Chiral Amido[4]resorcinarenes

Bruno Botta,*[a] Andrea Tafi,*[b] Fabiana Caporuscio,[a] Maurizio Botta,[b] Laura Nevola,[a] Ilaria D'Acquarica,[a] Caterina Fraschetti,[a] and Maurizio Speranza*[a]

Abstract: Diastereomeric proton-bound complexes formed between (*R*)- and (*S*)-amphetamine and some chiral amido[4]resorcinarene receptors display significant enantioselectivities when reacting with the enantiomers of 2-aminobutane in the gas phase. The origins of the measured enantioselectivities are discussed in the light of molecular mechanics calculations and molecular dynamics simulations and are ascribed to a combination of structural and dynamic factors, including the lengths and the isomeric structures of the host asymmetric pendants and the frequencies and amplitudes of their motion, as well as those of the proton-bonded amphetamine guests. The emerging picture may represent a starting point for deeper comprehension of the factors determining the different affinities of (*R*)- and (*S*)-amphetamine towards various chiral receptors, their selective binding to the monoamine transporters, and their sensitivity to specific inorganic ions.

Keywords: enantioselectivity · enzyme mimics · gas-phase reactions · kinetics · mass spectrometry

Introduction

Amphetamine (A) and its analogues are central nervous system stimulants. These compounds each contain a chiral centre, and their enantiomers show different pharmacological properties. Both (*S*)-(+)-amphetamine (D-amphetamine, $A_{(S)}$) and (*R*)-(−)-amphetamine (L-amphetamine, $A_{(R)}$) are thought to exert their effects by binding to the monoamine transporters and increasing extracellular levels of the biogenic amines, such as dopamine, norepinephedrine and serotonin.[1] It is hypothesized that $A_{(S)}$ acts primarily on the dopaminergic systems,[2–4] while $A_{(R)}$ is comparatively norepinephrinergic.[2,5] In all instances, the mechanisms of action of $A_{(S)}$ and $A_{(R)}$ proceed through preliminary interactions with the amino acids of the N terminus of human dopamine transporter (or their phosphorylated forms).[6] The dopamine transporter is a member of the Na^+- and Cl^--dependent plasma membrane transporters, which enable the transport of substrate together with Na^+ and Cl^- co-substrates.[7]

In view of the complexities of the uptake process depicted above, it would be of interest to investigate the natures of the noncovalent interactions between $A_{(S)}$ and $A_{(R)}$ and some artificial receptors containing different amino acidic groups in the gas phase under conditions mimicking the extensive desolvation accompanying the uptake of amphetamine inside the receptor cavity. In addition, one needs to evaluate the effects of specific inorganic ions, including Cl^-, on the substrate recognition step that impacts the entire uptake process.[8–10]

We have recently been engaged in extensive mass spectrometric (MS) studies of the interactions between some representative chiral biomolecules (C) and specifically designed chiral macrocyclic receptors (M), such as the amido[4]resorcinarene $\mathbf{1}_{(S)}$ (Figure 1),[11–15] in the gas phase, where interference from the solvent and the counterion is excluded. The molecular asymmetry of the selected hosts M is due to the four dissymmetric pendants, which may be spatially oriented

[a] Prof. B. Botta, Dr. F. Caporuscio, Dr. L. Nevola, Dr. I. D'Acquarica, Dr. C. Fraschetti, Prof. M. Speranza
Dipartimento degli Studi di Chimica
e Tecnologia delle Sostanze Biologicamente Attive
Università "La Sapienza", 00185 Roma (Italy)
Fax: (+39) 06-49913602
E-mail: maurizio.speranza@uniroma1.it

[b] Prof. A. Tafi, Prof. M. Botta
Dipartimento Farmaco Chimico Tecnologico
Università di Siena
53100 Siena (Italy)

Supporting information for this article is available on the WWW under http://www.chemeurj.org/ or from the author.

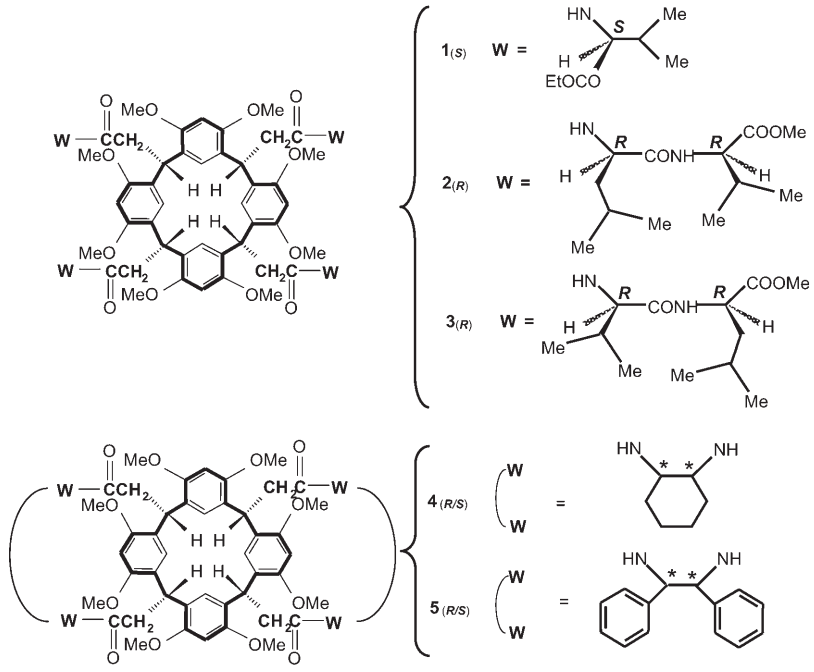

Figure 1. Selected amido[4]resorcinarenes **1**–**5.** The asterisks denote the configurations of the chiral centres: either *R*,*R* (for $\mathbf{4}_{(R)}$ and $\mathbf{5}_{(R)}$) or *S*,*S* (for $\mathbf{4}_{(S)}$ and $\mathbf{5}_{(S)}$).

so as to generate chiral cavities of different size and shape.[13] The enantioselectivities of the selected M hosts towards the C enantiomers were checked by introducing the proton-bonded two-body complexes $[M{\cdot}H{\cdot}C]^+$ into a Fourier Transform Ion Cyclotron Resonance Mass Spectrometer (FT-ICR-MS), fitted with an electrospray ionization source (ESI), and by measuring the rate of the displacement reaction (1) [Eq. (1)], where B is either (*R*)-(−)-but-2-ylamine ($B_{(R)}$) or (*S*)-(+)-but-2-ylamine ($B_{(S)}$).

$$[M \cdot H \cdot C]^+ + B \rightarrow [M \cdot H \cdot B]^+ + C \quad (1)$$

Abstract in Italian: *I complessi diastereomerici fra alcuni ammido[4]resorcinareni protonati chirali e la (*R*)- e (*S*)-anfetamina mostrano una notevole enantioselettività nella reazione con gli enantiomeri del 2-ammino butano in fase gassosa. L'origine della enantioselettività osservata viene discussa alla luce di calcoli di meccanica molecolare e di simulazioni di dinamica molecolare ed è attribuita alla combinazione di fattori strutturali e dinamici, come la lunghezza e la struttura isomerica dei pendagli della molecola ospite e la frequenza e l'ampiezza delle loro oscillazioni, così come di quelle dell'anfetamina legata al resorcinarene mediante un protone. Il quadro che emerge può rappresentare un punto di partenza per una comprensione più profonda dei fattori che determinano la diversa affinità della (*R*)- e (*S*)-anfetamina verso vari recettori chirali, la loro tendenza a legarsi selettivamente a trasportatori di monoammine, e la loro sensibilità nei confronti di specifici ioni inorganici.*

The same kinetic approach is employed in this paper in order to gather some insights into the specific interactions between A and several chiral macrocyclic hosts, containing either flexible (that is, **1**–**3**) or rigid (that is, **4** and **5**) pendants (Figure 1). The relevant kinetic results are discussed in the light of Molecular Mechanics (MM) calculations and Molecular Dynamics (MD) simulations and compared with those obtained in previous related studies.

Results and Discussion

FT-ICR experiments: The proton-bound complexes $[M{\cdot}H{\cdot}A]^+$ were generated in the FT-ICR-MS by electrospraying of M/A methanolic solutions. The same complexes are formed together with proton-bound $[M{\cdot}H{\cdot}(A)_2{\cdot}HCl]^+$ aggregates from ESI of $M/AH^+{\cdot}Cl^-$ methanolic solutions. The reaction between $[M{\cdot}H{\cdot}A]^+$ and amines B leads to the exclusive formation of the guest-exchange product $[M{\cdot}H{\cdot}B]^+$ [Eq. (2)], while that with $[M{\cdot}H{\cdot}(A)_2{\cdot}HCl]^+$ proceeds through a consecutive B-to-A displacement sequence with formation of the $[M{\cdot}H{\cdot}A{\cdot}B{\cdot}HCl]^+$ and $[M{\cdot}H{\cdot}(B)_2{\cdot}HCl]^+$ products [Eqs. (3) and (4)].

$$[M \cdot H \cdot A]^+ + B \rightarrow [M \cdot H \cdot B]^+ + A \quad (2)$$

$$[M \cdot H \cdot (A)_2 \cdot HCl]^+ + B \rightarrow [M \cdot H \cdot A \cdot B \cdot HCl]^+ + A \quad (3)$$

$$[M \cdot H \cdot A \cdot B \cdot HCl]^+ + B \rightarrow [M \cdot H \cdot (B)_2 \cdot HCl]^+ + A \quad (4)$$

The pseudo-first-order rate constants (k') of reactions 2 and 3 were obtained from the slopes of the relevant $\ln(I/I_0)$ versus t plots, where I is the signal intensity of the corresponding starting complex at the delay time t, and I_0 is the sum of the signal intensities of the starting complex and its products. The pseudo-first-order rate constant of step 4 was derived by best-fitting the relative abundance of the $[M{\cdot}H{\cdot}(A)_{2-n}{\cdot}B_n{\cdot}HCl]^+$ ($n=0$–2) ions as a function of the delay time t, using as the only constraint the k' value obtained for step 3 from the relevant $\ln(I/I_0)$ versus t plot. The second-order rate constants—$k=k'/[B]$—are denoted according to the configurations of the A, M and B molecules. Thus, k_{homo} refers to the complex in which A and M have the same configuration and k_{hetero} to that in which A and M have opposite configurations. The $k_{(R)}$ constant refers to the reaction with $B_{(R)}$ and the $k_{(S)}$ one to that with $B_{(S)}$.

Enantioselectivity is defined by the $\rho = k_{homo}/k_{hetero}$ ratio, when referred to the configuration of the M/A pair, or by the $\xi = k_{(R)}/k_{(S)}$ one, where the subscripts indicate the configuration of the amine B. A value of $\rho > 1$ indicates that the B-to-A displacement is faster in the homochiral complex than in the heterochiral one. The opposite is true when $\rho < 1$. A value of $\rho = 1$ corresponds to equal displacement rates. Analogously, a value of $\xi > 1$ indicates that the displacement of the A guest from a given complex is faster with the (*R*)-amine ($B_{(R)}$) than with the (*S*)-amine ($B_{(S)}$). Again, the opposite is true when $\xi < 1$. A value of $\xi = 1$ corresponds to equal displacement rates.

Irrespective of the starting methanolic solution, whether containing the free A base or its $AH^+ \cdot Cl^-$ hydrochloride, the ESI-formed $[M \cdot H \cdot A]^+$ complex always exhibits the same exchange rate constant. This suggests that the same $[M \cdot H \cdot A]^+$ structure is formed both from the free A and from the $AH^+ \cdot Cl^-$ precursors. Linear rate plots are invariably observed in the reactions between the B enantiomers and all the selected $[M \cdot H \cdot A]^+$ [Eq. (2); corr. coeff. $0.982 < r^2 < 0.999$) and $[M \cdot H \cdot (A)_2 \cdot HCl]^+$ complexes [Eq. (3); corr. coeff. $0.989 < r^2 < 0.999$) (see Figures A1–A20 in the Supporting Information (SI)). This common kinetic behaviour points to a single isomeric structure for both the $[M \cdot H \cdot A]^+$ and the $[M \cdot H \cdot (A)_2 \cdot HCl]^+$ complexes.[11–17]

The second-order rate constants (k) for all the displacement reactions 2–4 investigated are listed in Table 1. Their values, compared with the relevant collision rate constant (k_C),[18] provide a measure of the efficiency of the reaction (eff $= k/k_C$).

With regard to the exchange reaction 2, the $[M \cdot H \cdot A]^+$ complexes with M = $\mathbf{1}_{(S)}$ and $\mathbf{3}_{(R)}$ show the greatest enantioselectivity, with the homochiral complexes reacting from 1.82 to 2.57 times more slowly than the heterochiral ones. The opposite is true for the $[M \cdot H \cdot A]^+$ complexes with M = $\mathbf{2}_{(R)}$, **4** and **5** (here only with $B_{(R)}$). In general, the effect of the configuration of B on the reaction kinetics is not very pronounced ($0.82 < \xi < 1.25$). Base-induced loss of the first A molecule from the $[M \cdot H \cdot (A)_2 \cdot HCl]^+$ adducts [Eq. (3)] is faster (up to five times) than the loss of the same molecule from the corresponding $[M \cdot H \cdot A]^+$ complexes [Eq. (2)]. Reaction 3 displays significant enantioselectivity only when the diastereomeric $[\mathbf{3}_{(R)} \cdot H \cdot (A)_2 \cdot HCl]^+$ complexes are involved. As with $[\mathbf{3}_{(R)} \cdot H \cdot A]^+$, the homochiral $[\mathbf{3}_{(R)} \cdot H \cdot (A_{(R)})_2 \cdot HCl]^+$ complex reacts around 1.5 times more slowly than the heterochiral $[\mathbf{3}_{(R)} \cdot H \cdot (A_{(S)})_2 \cdot HCl]^+$ one. All the other $[M \cdot H \cdot (A)_2 \cdot HCl]^+$ congeners, except for $[\mathbf{2}_{(R)} \cdot H \cdot (A)_2 \cdot HCl]^+$ with $B_{(S)}$ ($\rho = 1.87 \pm 0.18$), show less pronounced enantioselectivities ($1.00 < \rho < 1.23$). In general, the enantioselectivity of $[M \cdot H \cdot (A)_2 \cdot HCl]^+$ is higher with $B_{(S)}$

Table 1. Exchange rate constants ($k \times 10^{-10}$ cm^3 molecule^{-1} s^{-1}).

Host	Complex	(*R*)-(−)-$C_4H_9NH_2$	ρ	(*S*)-(+)-$C_4H_9NH_2$	ρ	ξ	Reaction efficiency[a]	
		$k_{(R)}$	k_{homo}/k_{hetero}	$k_{(S)}$	k_{homo}/k_{hetero}	$k_{(R)}/k_{(S)}$	$k_{(R)}/k_C$	$k_{(S)}/k_C$
$\mathbf{1}_{(S)}$	$[\mathbf{1}_{(S)} \cdot H \cdot A]^+_{hetero}$	1.03 ± 0.03	0.39 ± 0.02	0.83 ± 0.03	0.45 ± 0.02	1.23 ± 0.09	0.09	0.07
	$[\mathbf{1}_{(S)} \cdot H \cdot A]^+_{homo}$	0.40 ± 0.01		0.37 ± 0.01		1.09 ± 0.03	0.03	0.03
	$[\mathbf{1}_{(S)} \cdot H \cdot (A)_2 \cdot HCl]^+_{hetero}$	1.84 ± 0.01	1.08 ± 0.03	1.42 ± 0.06	1.20 ± 0.09	1.30 ± 0.03	0.16	0.12
	$[\mathbf{1}_{(S)} \cdot H \cdot (A)_2 \cdot HCl]^+_{homo}$	1.99 ± 0.04		1.70 ± 0.06		1.17 ± 0.07	0.17	0.15
	$[\mathbf{1}_{(S)} \cdot H \cdot A \cdot B \cdot HCl]^+_{hetero}$	0.97	0.99	0.62	1.35	1.56	0.08	0.05
	$[\mathbf{1}_{(S)} \cdot H \cdot A \cdot B \cdot HCl]^+_{homo}$	0.96		0.84		1.14	0.08	0.07
$\mathbf{2}_{(R)}$	$[\mathbf{2}_{(R)} \cdot H \cdot A]^+_{hetero}$	1.11 ± 0.03	1.05 ± 0.05	1.14 ± 0.01	1.26 ± 0.04	0.97 ± 0.04	0.09	0.10
	$[\mathbf{2}_{(R)} \cdot H \cdot A]^+_{homo}$	1.17 ± 0.02		1.42 ± 0.02		0.82 ± 0.05	0.10	0.12
	$[\mathbf{2}_{(R)} \cdot H \cdot (A)_2 \cdot HCl]^+_{hetero}$	1.81 ± 0.03	1.05 ± 0.02	1.07 ± 0.05	1.87 ± 0.18	1.69 ± 0.11	0.15	0.09
	$[\mathbf{2}_{(R)} \cdot H \cdot (A)_2 \cdot HCl]^+_{homo}$	1.91 ± 0.02		2.00 ± 0.09		0.95 ± 0.06	0.16	0.17
	$[\mathbf{2}_{(R)} \cdot H \cdot A \cdot B \cdot HCl]^+_{hetero}$	0.96	0.73	0.80	0.99	1.20	0.09	0.07
	$[\mathbf{2}_{(R)} \cdot H \cdot A \cdot B \cdot HCl]^+_{homo}$	0.70		0.79		0.88	0.06	0.07
$\mathbf{3}_{(R)}$	$[\mathbf{3}_{(R)} \cdot H \cdot A]^+_{hetero}$	1.50 ± 0.01	0.55 ± 0.02	1.54 ± 0.02	0.51 ± 0.01	0.97 ± 0.02	0.13	0.13
	$[\mathbf{3}_{(R)} \cdot H \cdot A]^+_{homo}$	0.82 ± 0.02		0.78 ± 0.01		1.05 ± 0.04	0.07	0.07
	$[\mathbf{3}_{(R)} \cdot H \cdot (A)_2 \cdot HCl]^+_{hetero}$	4.14 ± 0.08	0.68 ± 0.02	4.48 ± 0.13	0.66 ± 0.04	0.92 ± 0.05	0.36	0.38
	$[\mathbf{3}_{(R)} \cdot H \cdot (A)_2 \cdot HCl]^+_{homo}$	2.82 ± 0.02		2.94 ± 0.09		0.96 ± 0.04	0.24	0.25
	$[\mathbf{3}_{(R)} \cdot H \cdot A \cdot B \cdot HCl]^+_{hetero}$	1.61	0.71	1.73	0.60	0.93	0.14	0.15
	$[\mathbf{3}_{(R)} \cdot H \cdot A \cdot B \cdot HCl]^+_{homo}$	1.14		1.02		1.12	0.10	0.09
$\mathbf{4}_{(R)}$ and $\mathbf{4}_{(S)}$	$[\mathbf{4} \cdot H \cdot A_{(R)}]^+_{hetero}$	1.70 ± 0.07	1.12 ± 0.09	1.62 ± 0.07	1.14 ± 0.09	1.05 ± 0.07	0.14	0.14
	$[\mathbf{4} \cdot H \cdot A_{(R)}]^+_{homo}$	1.90 ± 0.07		1.85 ± 0.06		1.03 ± 0.04	0.16	0.16
	$[\mathbf{4} \cdot H \cdot (A_{(R)})_2 \cdot HCl]^+_{hetero}$	3.87 ± 0.07	1.11 ± 0.04	3.79 ± 0.05	1.00 ± 0.03	1.02 ± 0.03	0.33	0.32
	$[\mathbf{4} \cdot H \cdot (A_{(R)})_2 \cdot HCl]^+_{homo}$	4.30 ± 0.08		3.79 ± 0.06		1.13 ± 0.04	0.37	0.32
	$[\mathbf{4} \cdot H \cdot A_{(R)} \cdot B \cdot HCl]^+_{hetero}$	1.04	1.26	1.15	1.27	0.90	0.09	0.10
	$[\mathbf{4} \cdot H \cdot A_{(R)} \cdot B \cdot HCl]^+_{homo}$	1.31		1.46		0.90	0.11	0.12
$\mathbf{5}_{(R)}$ and $\mathbf{5}_{(S)}$	$[\mathbf{5} \cdot H \cdot A_{(R)}]^+_{hetero}$	1.06 ± 0.02	1.26 ± 0.09	1.17 ± 0.04	0.91 ± 0.06	0.91 ± 0.05	0.09	0.10
	$[\mathbf{5} \cdot H \cdot A_{(R)}]^+_{homo}$	1.34 ± 0.05		1.07 ± 0.03		1.25 ± 0.09	0.11	0.09
	$[\mathbf{5} \cdot H \cdot (A_{(R)})_2 \cdot HCl]^+_{hetero}$	3.05 ± 0.11	1.16 ± 0.05	2.60 ± 0.03	1.23 ± 0.03	1.17 ± 0.06	0.26	0.22
	$[\mathbf{5} \cdot H \cdot (A_{(R)})_2 \cdot HCl]^+_{homo}$	3.54 ± 0.02		3.20 ± 0.03		1.11 ± 0.01	0.30	0.27
	$[\mathbf{5} \cdot H \cdot A_{(R)} \cdot B \cdot HCl]^+_{hetero}$	0.71	1.15	0.68	0.94	1.04	0.06	0.06
	$[\mathbf{5} \cdot H \cdot A_{(R)} \cdot B \cdot HCl]^+_{homo}$	0.82		0.64		1.28	0.07	0.05

[a] Reaction efficiency expressed by the ratio between the measured rate constants and the corresponding collision constant k_C, calculated by the trajectory calculation method (Ref. [18]).

($0.66 < \rho < 1.87$) than with $B_{(R)}$ ($0.68 < \rho < 1.16$). The effect of the configuration of B on the first steps [Eq. (3)] of the exchange reaction sequences [Eq. (3), Eq. (4)] is appreciable, with $[M{\cdot}H{\cdot}(A)_2{\cdot}HCl]^+$ [$M = \mathbf{1}_{(S)}$ ($1.17 < \xi < 1.30$) and $\mathbf{2}_{(R)}$ ($0.95 < \xi < 1.69$)]. All the other $[M{\cdot}H{\cdot}(A)_2{\cdot}HCl]^+$ congeners show a relatively minor sensitivity to the B configuration ($0.92 < \xi < 1.17$). Base-induced loss of the residual A molecule from the $[M{\cdot}H{\cdot}A{\cdot}B{\cdot}HCl]^+$ adducts [Eq. (4)] is normally up to five times slower than the loss of the first A molecule from the $[M{\cdot}H{\cdot}(A)_2{\cdot}HCl]^+$ adducts [Eq. (3)]. However, reaction 4 displays an enantioselectivity that can be qualitatively and quantitatively different from that exhibited by the preceding step [Eq. (3)]. For instance, the ρ values measured with the diastereomeric $[\mathbf{4}{\cdot}H{\cdot}A_{(R)}{\cdot}B{\cdot}HCl]^+$ complexes amount to ca. 1.3, whereas those obtained for their $[\mathbf{4}{\cdot}H{\cdot}(A_{(R)})_2{\cdot}HCl]^+$ precursors do not exceed 1.1. In addition, $\rho < 1$ values are invariably measured with the diastereomeric $[\mathbf{2}_{(R)}{\cdot}H{\cdot}A{\cdot}B{\cdot}HCl]^+$ complexes, whereas $\rho > 1$ values were obtained with their $[\mathbf{2}_{(R)}{\cdot}H{\cdot}(A)_2{\cdot}HCl]^+$ precursors.

In view of the different efficiencies and selectivities of the base-induced reactions 2–4, reported in Table 1, the question arises as to their origin, whether due to kinetic factors (that is, related to the effects of the M host chiral frame upon the displacement transition structures), or to thermodynamic factors (that is, just reflecting the relative stabilities of the diastereomeric $[M{\cdot}H{\cdot}A]^+$, $[M{\cdot}H{\cdot}(A)_2{\cdot}HCl]^+$ and $[M{\cdot}H{\cdot}A{\cdot}B{\cdot}HCl]^+$ complexes). A detailed structural and energetic analysis of a representative proton-bonded diastereomeric $[M{\cdot}H{\cdot}A]^+$, $[M{\cdot}H{\cdot}(A)_2{\cdot}HCl]^+$ and $[M{\cdot}H{\cdot}A{\cdot}B{\cdot}HCl]^+$ adducts is needed in order to answer this important question. This task has been undertaken with the aid of Molecular Mechanics (MM) calculations and Molecular Dynamics (MD) simulations.

MM and MD calculations on diastereomeric $[\mathbf{1}_{(S)}{\cdot}H{\cdot}(A)_{n+1}{\cdot}(HCl)_n]^+$ (n=0,1) complexes: As pointed out in a previous study,[12] a quantitative estimate of the energetics of the $[\mathbf{1}_{(S)}{\cdot}H{\cdot}A]^+$ and $[\mathbf{1}_{(S)}{\cdot}H{\cdot}(A)_2{\cdot}HCl]^+$ aggregates by MM calculations and MD simulations is prevented because of the flexibility of the M host, which makes the number of its conceivable adducts with amphetamine exceedingly large. Besides, any computational attempt to reproduce quantitatively the small activation free energy differences derived from the measured enantioselectivity values ($< 2.3\ kJ\,mol^{-1}$ at 300 K; Table 1) is thwarted by the relatively large uncertainty associated with the computational approaches. As a consequence, we provide a description of the structural features of the $[\mathbf{1}_{(S)}{\cdot}H{\cdot}A]^+$ and $[\mathbf{1}_{(S)}{\cdot}H{\cdot}(A)_2{\cdot}HCl]^+$ aggregates that may be of some help in rationalizing the FT-ICR experimental results.

As illustrated in the Experimental Section, a complete and reasonably homogeneous sampling of the whole potential energy hypersurface of the selected systems is better attained through the combination of Monte Carlo (MC) docking studies with constant temperature MD simulations. The time evolution of the molecular motions of the host and guest moieties would in fact be expected to let the system move among many conformations populated at room temperature, by crossing over low energy barriers and by favouring large flat minima with respect to narrow ones, so as to provide a dynamic picture of the recognition process.

Figure 2a,b shows the results of MCMM/MOLS and MCMM/LMCS/MOLS docking studies on the homochiral $[\mathbf{1}_{(S)}{\cdot}H{\cdot}A_{(S)}]^+$ and the heterochiral $[\mathbf{1}_{(S)}{\cdot}H{\cdot}A_{(R)}]^+$ complexes, respectively. An intermolecular out-of-plane bending is used as a structural descriptor (SD_1; see Figure 11 in the Experimental section) to classify the overall geometries of the low-energy complexes. Figure 2b indicates that the $A_{(R)}$ guest is "better" hosted in the $[\mathbf{1}_{(S)}{\cdot}H{\cdot}A_{(R)}]^+$ complex (in terms of static shape and electrostatic complementarities) in a region of three-dimensional space at SD_1 values close to 0°: that is, in the *ext* region of the host between two adjacent L-valinamido pendants (Figure 3a).

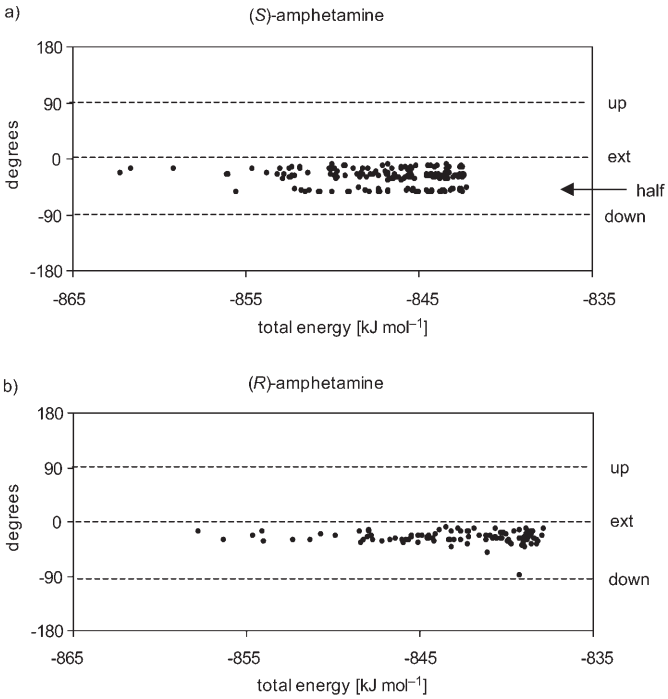

Figure 2. Docking of $[\mathbf{1}_{(S)}{\cdot}H{\cdot}A_{(S)}]^+$ (a) and $[\mathbf{1}_{(S)}{\cdot}H{\cdot}A_{(R)}]^+$ (b).

A similar position is preferentially occupied by the $A_{(S)}$ guest in the homochiral $[\mathbf{1}_{(S)}{\cdot}H{\cdot}A_{(S)}]^+$ complex (Figures 2a and 3b). However, some of the more energetic $[\mathbf{1}_{(S)}{\cdot}H{\cdot}A_{(S)}]^+$ structures present the guest in a region of three-dimensional space at SD_1 values around −50°: that is, "halfway" between the *ext* and the *down* regions of the host (henceforth denoted as the *half* region). In these structures, the phenyl ring of the guest molecule is positioned inside the lower cavity of the host among the chiral pendants (Figures 2a and 3c). With regard to the 0 K average energies of the two diastereomeric structures, the homochiral $[\mathbf{1}_{(S)}{\cdot}H{\cdot}A_{(S)}]^+$ complex is about $4\ kJ\,mol^{-1}$ more stable than the heterochiral

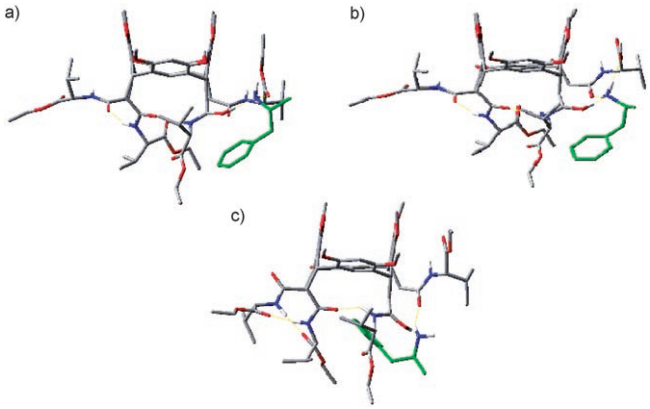

Figure 3. Monte Carlo global minimum geometries of the $[\mathbf{1}_{(S)}\cdot H\cdot A_{(R)}]^+$ (a) and $[\mathbf{1}_{(S)}\cdot H\cdot A_{(S)}]^+$ (b) complexes, showing the preferred accommodation of the A guest to the *ext* region of the complex. c) Geometry of the *half*-$[\mathbf{1}_{(S)}\cdot H\cdot A_{(S)}]^+$ complex, showing the phenyl ring of the guest molecule positioned inside the host cavity.

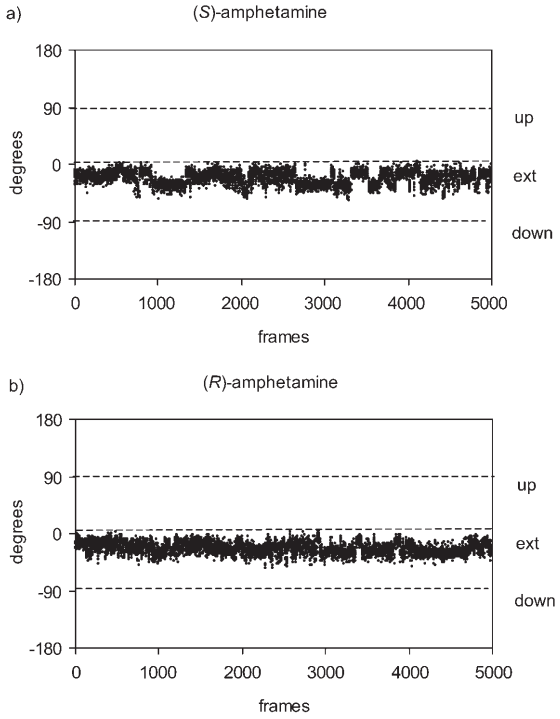

Figure 4. Molecular dynamics (SD_1 vs. frames) of *ext*-$[\mathbf{1}_{(S)}\cdot H\cdot A_{(S)}]^+$ (a) and *ext*-$[\mathbf{1}_{(S)}\cdot H\cdot A_{(R)}]^+$ (b).

$[\mathbf{1}_{(S)}\cdot H\cdot A_{(R)}]^+$ adduct, probably due to a more favourable orientation of the methyl group, directed toward the protonated pendant (cf. Figure 3a and b).

The results of MD simulations, starting from relevant *ext* minima of $[\mathbf{1}_{(S)}\cdot H\cdot A_{(S)}]^+$ (Figure 4a) and $[\mathbf{1}_{(S)}\cdot H\cdot A_{(R)}]^+$ (Figure 4b), suggest that, at 300 K, the amphetamine guest is permanently trapped at the *ext* region of the host close to its chiral lower rim. As to the relative stability of *ext*-$[\mathbf{1}_{(S)}\cdot H\cdot A_{(S)}]^+$ vs. *ext*-$[\mathbf{1}_{(S)}\cdot H\cdot A_{(R)}]^+$ structures, MD simulations confirm the above qualitative order, though mostly due to entropy factors. Indeed, a comparative inspection of Figure 4a and b reveals some more scattering in the SD_1 values of $[\mathbf{1}_{(S)}\cdot H\cdot A_{(S)}]^+$, relative to those of $[\mathbf{1}_{(S)}\cdot H\cdot A_{(R)}]^+$. In order to clarify the structural reasons for such a scattering, a second structural descriptor—SD_2—has been defined (see Figure 11, Experimental Section), describing the orientation of the guest phenyl ring with respect to the facing aromatic ring of the host. When the frequencies of the values taken by SD_2 during the MD runs are plotted against the values themselves (Figure 5), it becomes obvious that the SD_1 oscillations of Figure 4a correspond to upside down turns of the guest.

The more frequent and complete oscillations of the guest in the homochiral $[\mathbf{1}_{(S)}\cdot H\cdot A_{(S)}]^+$ structure, attested to by the smoother distribution of SD_2 values (Figure 5, bottom), suggest the idea of a higher density of rotational states for the $\mathbf{A}_{(S)}$ guest in the homochiral $[\mathbf{1}_{(S)}\cdot H\cdot A_{(S)}]^+$ structure, relative to $A_{(R)}$ in the heterochiral $[\mathbf{1}_{(S)}\cdot H\cdot A_{(R)}]^+$ one (Figure 5, top).[19] The phenomenon reflects the different host–guest interaction pattern at the guest chiral centre (see Ref. [19]). It is concluded that the homochiral $[\mathbf{1}_{(S)}\cdot H\cdot A_{(S)}]^+$ structure benefits from a greater rotational freedom—relative to the heterochiral $[\mathbf{1}_{(S)}\cdot H\cdot A_{(R)}]^+$ one—and, therefore, from a greater entropic content.

Figure 6a and b sum up the results of MCMM/MOLS and MCMM/LMCS/MOLS docking calculations on the homochiral $[\mathbf{1}_{(S)}\cdot H\cdot(A_{(S)})_2\cdot HCl]^+$ and the heterochiral $[\mathbf{1}_{(S)}\cdot H\cdot(A_{(R)})_2\cdot HCl]^+$ complexes, respectively. They display the pattern of values taken by couples of SD_1 intermolecular descriptors, each one relating to the orientation of one amphetamine molecule. The lowest-energy MC $[\mathbf{1}_{(S)}\cdot H\cdot(A)_2\cdot HCl]^+$ structures, collected within 20 kJ mol^{-1}, are characterized by the AH^+/Cl^- pair being preferentially located either in the *down* or in the *ext* position (red dots in Figure 6). At the same time, the neutral amphetamine molecule is hosted in close proximity to the hydrochloride (either in the *down* or in the *ext* regions; black dots in Figure 6). When the hydrochloride is hosted at the lower rim (*down* position), the neutral amphetamine can also reside either in the *ext* region or at the upper rim of the host (the *up* region). The $[\mathbf{1}_{(S)}\cdot H\cdot(A)_2\cdot HCl]^+$ structures with both the A molecule and the AH^+/Cl^- pair in the *ext* region are denoted as *ext-ext*. Those with both the A molecule and the AH^+/Cl^- pair in the *down* region are denoted as *down–down*. Those with the A molecule in the *ext* position and the AH^+/Cl^- pair in the *down* one are denoted as *down-ext*. Those with the A molecule in the *up* position and the AH^+/Cl^- pair in the *down* one are denoted as *down–up* (see Figures S1–S8 in the Supporting Information). The data shown in Figure 6a, b point to very limited differences of the 0 K steric energies among the four possible geometries of the diastereomeric complexes ($\Delta E \leq 4.0$ kJ mol^{-1}), with the *down-ext* and *ext-ext* structures as the most stable ones (see Table 2). This means that, according to the Amber* force field, the four detected geometries should all be populated if thermal excitation (entropy) did not come into play.

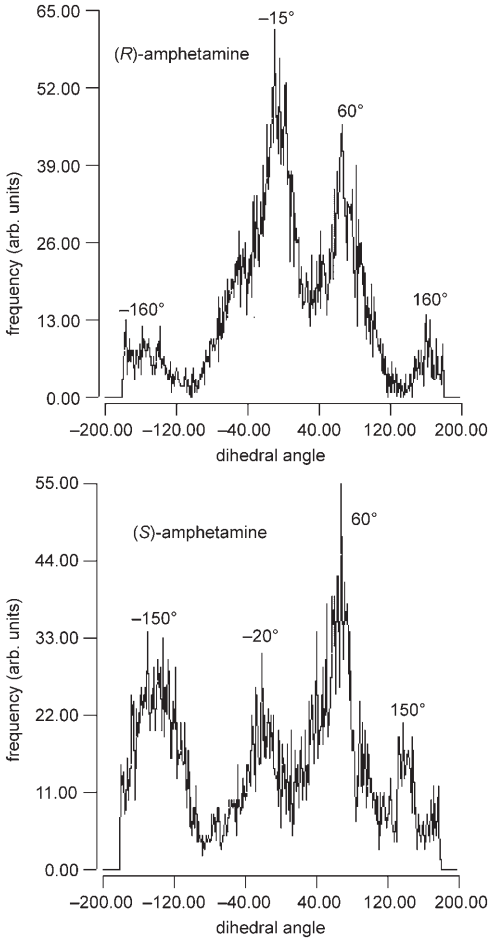

Figure 5. Frequency plots of MD simulations showing the oscillations of A in *ext*-[$\mathbf{1}_{(S)}$·H·A]$^+$. Maxima at −15°/−20° and 60° correspond to "*up*" orientations of the phenyl ring of the guest (more populated in both cases). Maxima at −160°/−150° and 160°/150° correspond to "*down*" orientations of the phenyl ring (differently populated in the two diastereomeric complexes).

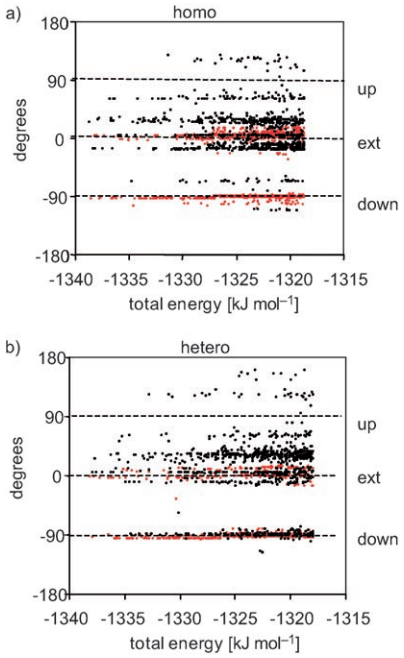

Figure 6. Docking of the homochiral [$\mathbf{1}_{(S)}$·H·$(A_{(S)})_2$·HCl]$^+$ (a) and the heterochiral [$\mathbf{1}_{(S)}$·H·$(A_{(R)})_2$·HCl]$^+$ complex (b). The red dots refer to the positions of the AH$^+$/Cl$^-$ pair; the black dots refer to the positions of the neutral A molecule.

Table 2. Computed relative energetics of the [$\mathbf{1}_{(S)}$·H·A_2·HCl]$^+$ regioisomers.

Complex	Geometry	Docking Output number	(Steric energy) ΔE [kJ mol^{-1}]
[$\mathbf{1}_{(S)}$·H·$(A_{(R)})_2$·HCl]$^+$	*ext-ext*	1	0.0
	down-ext	2	0.2
	down-up	11	2.5
	down-down	20	3.5
[$\mathbf{1}_{(S)}$·H·$(A_{(S)})_2$·HCl]$^+$	*ext-ext*	2	0.4
	down-ext	1	0.0
	down-up	9	1.9
	down-down	22	4.0

Molecular dynamics simulations, performed at 300 K and starting from the lowest-energy *ext-ext* and *down-ext* minima of [$\mathbf{1}_{(S)}$·H·$(A_{(S)})_2$·HCl]$^+$ and [$\mathbf{1}_{(S)}$·H·$(A_{(R)})_2$·HCl]$^+$, suggest that, at this temperature, *ext-ext* geometries are at least a couple of kilocalories per mol less stable than *down-ext* minima (results not shown). Furthermore, they reveal that, at 300 K, the $A_{(R)}H^+/Cl^-$ pair in the heterochiral *down-ext*-[$\mathbf{1}_{(S)}$·H·$(A_{(R)})_2$·HCl]$^+$ structure remains firmly located in the *down* region, while the *ext* $A_{(R)}$ molecule can easily shift toward the *down* region. The nature of such a time-dependent event is illustrated in Figure 7. After 13 ns, the host pendant H-bonded to the $A_{(R)}$ molecule moves up towards the upper rim of the resorcin[4]arene. Through this movement, the guest finds the way to shift rapidly from the *ext* to the *down* position of the host simply through a torsion of the pendant, and locks itself into the *down* cavity by dragging the pendant along with it.

A similar, but fully reversible, motion has been observed in the MD simulation of the homochiral *down-ext*-[$\mathbf{1}_{(S)}$·H·$(A_{(S)})_2$·HCl]$^+$ structure (Figure 8). While the $A_{(S)}H^+/Cl^-$ pair stands still at the *down* region, the $A_{(S)}$ moiety moves after 19 ns from the *ext* to the *down* position in a fashion similar to that shown by $A_{(R)}$ in the heterochiral *down-ext*-[$\mathbf{1}_{(S)}$·H·$(A_{(R)})_2$·HCl]$^+$ structure, except that the movement is now reversed by the absence of the concurrent movement of a pendant.

As a whole, the results of the MD simulations suggest that, at 300 K, the *down-down* and *down-ext* forms are probably the most populated, easily interconverting [$\mathbf{1}_{(S)}$·H·$(A_{(S)})_2$·HCl]$^+$ regioisomers. As for the heterochiral [$\mathbf{1}_{(S)}$·H·$(A_{(R)})_2$·HCl]$^+$ complex, *down-down* is probably the most populated regioisomer, to which the *down-ext* one irreversibly isomerizes.

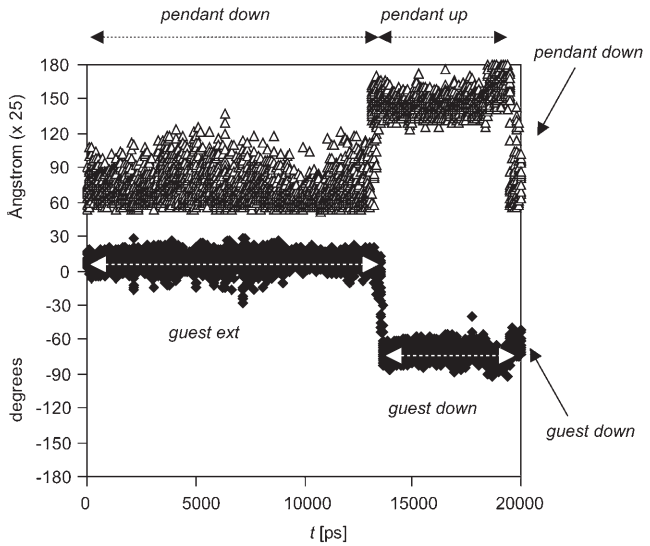

Figure 7. Molecular dynamics of the heterochiral *down-ext*-$[\mathbf{1}_{(S)}\cdot H\cdot(A_{(R)})_2\cdot HCl]^+$ structure. The $A_{(R)}$ molecule follows the movement of a chiral pendant of the host and moves *irreversibly* from the *ext* to the *down* region: △: Cl−···H-N-pendant distance (Å×25), ◆: improper SD_1 dihedral angle.

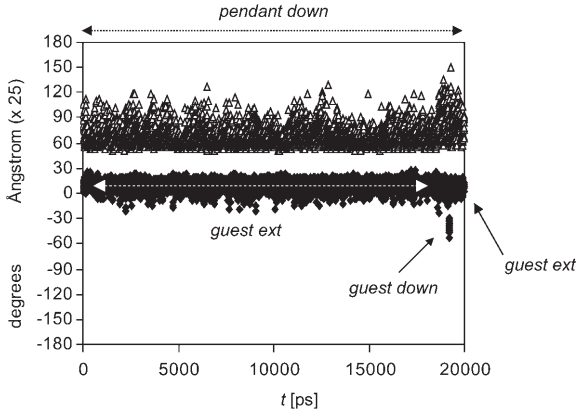

Figure 8. Molecular dynamics of the homochiral *down-ext*-$[\mathbf{1}_{(S)}\cdot H\cdot(A_{(S)})_2\cdot HCl]^+$ structure. The $A_{(S)}$ molecule moves *reversibly* from the *ext* to the *down* region; see Figure 7 for symbols.

Kinetics and enantioselectivities of the $[\mathbf{1}_{(S)}\cdot H\cdot(A)_{n+1}\cdot(HCl)_n]^+$ (n=0,1) complexes: Table 1 indicates that, irrespective of the B configuration, the heterochiral $[\mathbf{1}_{(S)}\cdot H\cdot A_{(R)}]^+$ complex invariably reacts more rapidly than the homochiral analogue ($\rho < 1$). Besides, while $B_{(R)}$ reacts more rapidly than $B_{(S)}$ with the heterochiral $[\mathbf{1}_{(S)}\cdot H\cdot A_{(R)}]^+$ complex ($\xi = 1.23 \pm 0.09$), they exhibit almost the same reactivity with the homochiral $[\mathbf{1}_{(S)}\cdot H\cdot A_{(S)}]^+$ adduct ($\xi = 1.09 \pm 0.03$). As pointed out above, Molecular Mechanics (MM) calculations and Molecular Dynamics (MD) simulations indicate that the proton-bound $A_{(S)}$ guest, although permanently located at the *ext* position of the host in $[\mathbf{1}_{(S)}\cdot H\cdot A]^+$, can rotate almost freely over the host's structure, whilst the proton-bound $A_{(R)}$ enantiomer can just oscillate over a restricted angle (Figure 5). This implies that the homochiral $[\mathbf{1}_{(S)}\cdot H\cdot A_{(S)}]^+$ *ext* structure is entropically stabilized relative to the heterochiral $[\mathbf{1}_{(S)}\cdot H\cdot A_{(R)}]^+$ complex. This may account *in part* for the measured $\rho < 1$ factors. The different dynamics of $[\mathbf{1}_{(S)}\cdot H\cdot A_{(S)}]^+$ vs $[\mathbf{1}_{(S)}\cdot H\cdot A_{(R)}]^+$ may play a role as well. The frequent and complete rotation of the $A_{(S)}$ guest in the homochiral $[\mathbf{1}_{(S)}\cdot H\cdot A_{(S)}]^+$ *ext* structure may slow down the B-to-A displacement process by hindering the accompanying proton transfer from $A_{(S)}$ to B. Similar hindrance is absent in the heterochiral $[\mathbf{1}_{(S)}\cdot H\cdot A_{(R)}]^+$ *ext* structure because of the restricted oscillation of the $A_{(R)}$ guest, which leaves the region of three-dimensional space adjacent to the upper rim of the host open to B. This dynamic picture may also account for the different ξ enantioselectivity factors measured for the diastereomeric $[\mathbf{1}_{(S)}\cdot H\cdot A]^+$ complexes.

Table 1 also reveals that the base-induced loss of the first A molecule from the $[\mathbf{1}_{(S)}\cdot H\cdot(A)_2\cdot HCl]^+$ adducts [Eq. (3)] is appreciably faster (up to 4.9 times) than loss of the same molecule from the corresponding $[\mathbf{1}_{(S)}\cdot H\cdot A]^+$ complexes [Eq. (2)]. This behaviour can be explained by the increased probability of the incoming B amine experiencing proton transfer from one of the two protonated centres of the $[\mathbf{1}_{(S)}\cdot H\cdot(A)_2\cdot HCl]^+$ structures. An additional factor might be the steric preference of the encumbered lower rim of the host, already occupied by the AH^+/Cl^- pair in the *down-down*-$[\mathbf{1}_{(S)}\cdot H\cdot(A)_2\cdot HCl]^+$ structure, to accommodate the small amine B rather than the second amphetamine A. The first B-to-A molecule displacement in $[\mathbf{1}_{(S)}\cdot H\cdot(A)_2\cdot HCl]^+$ is not particularly enantioselective ($\rho = 1.08 \pm 0.03$ ($B_{(R)}$); 1.20 ± 0.09 ($B_{(S)}$)). Such a poor enantioselectivity can be accounted for by the fact that in most $[\mathbf{1}_{(S)}\cdot H\cdot(A)_2\cdot HCl]^+$ isomers the chloride ion is located deep inside the lower rim of the host and strongly interacts with the AH^+ moiety. The neutral A molecule is instead located outside the chiral cavity of the host (the *down-ext* isomer) or inside the cavity (the *down-down* isomer), but in a position removed from its chiral centres because of the presence both of the chloride ion "spacer" and of the AH^+ moiety. This implies that the host is not able to exert any significant chiral discrimination either towards the neutral amphetamine molecule or towards the incoming 2-aminobutane reactant ($\rho \approx 1$ and $\xi \approx 1$).

Table 1 shows that the base-induced loss of the second A molecule from the $[\mathbf{1}_{(S)}\cdot H\cdot A\cdot B\cdot HCl]^+$ [Eq. (4)] is almost twice as slow as the loss of the first molecule from the corresponding $[\mathbf{1}_{(S)}\cdot H\cdot(A)_2\cdot HCl]^+$ complexes [Eq. (3)]. This behaviour can be explained by the fact that the reaction must involve proton transfer from the residual AH^+ moiety to the second B amine. Indeed, with the reasonable assumption of an indiscriminate proton transfer from $[\mathbf{1}_{(S)}\cdot H\cdot A\cdot B\cdot HCl]^+$ to B in the encounter complex, the probability of the reaction is exactly one half of that between $[\mathbf{1}_{(S)}\cdot H\cdot(A)_2\cdot HCl]^+$ and B. As in the case of the first B-to-A displacement in $[\mathbf{1}_{(S)}\cdot H\cdot(A)_2\cdot HCl]^+$, the further B-to-A molecule displacement in $[\mathbf{1}_{(S)}\cdot H\cdot A\cdot B\cdot HCl]^+$ is not particularly enantioselective [$\rho = 0.99$ ($B_{(R)}$); 1.35 ($B_{(S)}$)]. The reason for such limited enantioselectivity is the same: namely the presence of the

chloride ion "spacer" in $[\mathbf{1}_{(S)}\cdot H\cdot A\cdot B\cdot HCl]^+$, obliging the proton-bonded A guest to reside in a zone of the host away from its chiral centres.

Kinetics and enantioselectivities of the other $[M\cdot H\cdot(A)_{n+1}\cdot(HCl)_n]^+$ (n=0,1) complexes: Analysis of Table 1 reveals that lengthening of the chiral pendants of the host from L-valine ethyl ester ($\mathbf{1}_{(S)}$) to the D-leucyl-D-valine ($\mathbf{2}_{(R)}$) and D-valyl-D-leucine ($\mathbf{3}_{(R)}$) methyl esters has a significant effect on the kinetics and the enantioselectivities of the B-to-A displacements in the diastereomeric $[M\cdot H\cdot A]^+$ complexes. In particular, while the ρ enantioselectivity factors for the B-induced displacement in $[\mathbf{1}_{(S)}\cdot H\cdot A]^+$ [$\rho = 0.39\pm0.02$ ($B_{(R)}$); 0.45 ± 0.02 ($B_{(S)}$)] and in $[\mathbf{3}_{(R)}\cdot H\cdot A]^+$ [$\rho = 0.55\pm0.02$ ($B_{(R)}$); 0.51 ± 0.01 ($B_{(S)}$)] are wholly comparable, those for the same reaction with $[\mathbf{2}_{(R)}\cdot H\cdot A]^+$ are significantly different and close to unity [$\rho = 1.05\pm0.05$ ($B_{(R)}$); 1.26 ± 0.04 ($B_{(S)}$)]. This observation suggests that the most populated $[\mathbf{3}_{(R)}\cdot H\cdot A]^+$ structure strictly resembles the corresponding *ext*-$[\mathbf{1}_{(S)}\cdot H\cdot A]^+$ one, in which the A guest is proton-bonded to one of the valinamido carbonyls of the host (Figure 9). In $[\mathbf{2}_{(R)}\cdot H\cdot A]^+$, the same interaction instead connects the A moiety with the leucinamido carbonyls of the host. The different physical environment of the departing A in the B-to-A displacement may be responsible for the different ρ values between *ext*-$[\mathbf{2}_{(R)}\cdot H\cdot A]^+$ and the *ext*-$[\mathbf{1}_{(S)}\cdot H\cdot A]^+$/*ext*-$[\mathbf{3}_{(R)}\cdot H\cdot A]^+$ pair.

The effects of the lengths of the chiral pendants of the host also extend to the enantioselectivities of the B-to-A displacements in the diastereomeric $[M\cdot H\cdot(A)_2\cdot HCl]^+$ complexes. In particular, both the sequential base-induced losses of the A molecule from the $[\mathbf{3}_{(R)}\cdot H\cdot(A)_2\cdot HCl]^+$ adducts [Eqs. (3), (4)] are appreciably faster and more selective ($\rho = 0.68\pm0.02$ [Eq. (3)], 0.71 [Eq. (4)] ($B_{(R)}$); 0.66 ± 0.04 [Eq. (3)], 0.60 [Eq. (4)] ($B_{(S)}$)) than the same processes with $[\mathbf{1}_{(S)}\cdot H\cdot(A)_2\cdot HCl]^+$ and $[\mathbf{2}_{(R)}\cdot H\cdot(A)_2\cdot HCl]^+$ (Table 1). Such a significant enantioselectivity can be accounted for by the fact that in $[M\cdot H\cdot(A)_2\cdot HCl]^+$ the chloride ion occupies a position nearby the arrow in Figure 9 and therefore pushes the AH^+ moiety down to the host pendants (Figures S4 and S8 of the Supporting Information). Unlike in the diastereomeric $[\mathbf{1}_{(S)}\cdot H\cdot(A)_2\cdot HCl]^+$ structures, the proton-bonded A guests in the $[\mathbf{3}_{(R)}\cdot H\cdot(A)_2\cdot HCl]^+$ congeners are still close to the Cl^- "spacer", but now they are surrounded by the chiral leucine methyl ester tails. If they are instead surrounded by the less encumbered valine methyl ester ones, as in $[\mathbf{2}_{(R)}\cdot H\cdot(A)_2\cdot HCl]^+$, the enantioselectivity of the first B-to-A displacement is strongly reduced and even inverted [$\rho = 1.05\pm0.02$ ($B_{(R)}$); 1.87 ± 0.18 ($B_{(S)}$); Table 1], whereas that of the further B-to-A displacement is essentially unchanged.

Such a pronounced variability of the enantioselectivity factors as a function of the natures and the isomeric structures of the chiral pendants of the flexible **1**–**3** hosts does not find any correspondence in the family of the rigid hosts **4** and **5**. Here, in fact, both the measured ρ and ξ factors are close to unity (Table 1). A major reason for such different behaviour can be found in the "open" cavity of the host, caused by the specific position of the chiral cyclohexane (**4**) and diphenylethane (**5**) moieties placed at the largest distance from each other. With this rigid arrangement, the host is not able to exert any significant chiral discrimination either towards the amphetamine moiety or towards the incoming 2-aminobutane reactant.

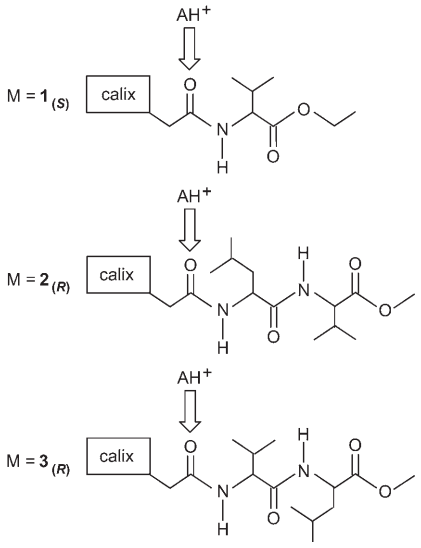

Figure 9. Most favoured proton-bond interactions between A and the pendants of M in the *ext*-$[M\cdot H\cdot A]^+$ complexes (M = **1**–**3**).

Conclusion

The experimental and computational results illustrated above shed some light on the specific noncovalent interactions operating between the amphetamine (A) enantiomers and the chiral amido[4]resorcinarene receptors M = **1**–**5**. They indicate that the gas-phase kinetics and enantioselectivities of the base-induced displacement reactions between the 2-aminobutane enantiomers (B) and the diastereomeric $[M\cdot H\cdot A]^+$ complexes are mainly determined by structural and dynamic factors, including the lengths and the isomeric structures of the host asymmetric pendants and the frequencies and the amplitudes of the oscillation of the proton-bonded A molecules in the *ext* region of the host. The same factors also determine the kinetics and the enantioselectivities of the B-induced displacement sequences on the diastereomeric $[M\cdot H\cdot(A)_2\cdot HCl]^+$ complexes. The presence of the chloride ion "spacers" strongly anchors the chiral A guests and keeps them away from the chiral centres of the host. The consequence is an increased B-to-A exchange rate, accompanied by reduced enantioselectivity. This effect is particularly evident with amido[4]resorcinarene hosts containing short L-valinamido pendants, such as $\mathbf{1}_{(S)}$. With those containing longer dipeptidic pendants, such as $\mathbf{2}_{(R)}$ and $\mathbf{3}_{(R)}$, the effect depends on the isomeric structures of the pendants themselves.

The dynamics of the diastereomeric $[M\cdot H\cdot(A)_2\cdot HCl]^+$ complexes may also play a role in determining chiral dis-

crimination of the amphetamine enantiomers. Thus, the *ext* $A_{(R)}$ molecule in the heterochiral *down-ext*-$[\mathbf{1}_{(S)}\cdot H\cdot(A_{(R)})_2\cdot HCl]^+$ structure may follow the movements of the chiral pendants of the host and move rapidly from the *ext* to the *down* region. In the same way, the *ext* $A_{(S)}$ molecule in the homochiral *down-ext*-$[\mathbf{1}_{(S)}\cdot H\cdot(A_{(S)})_2\cdot HCl]^+$ structure follows the same movement, which has been simulated as a fully reversible one. This is another case illustrating the importance of the structural flexibility of the receptor in determining differential conformational entropy penalties in their complexation with several inhibitors.[20,21]

This kinetic and dynamic study of tailor-made simplified models may be considered a starting point for deeper comprehension of the factors determining the different affinities of D- and L-amphetamine towards various chiral receptors, their selective binding to the monoamine transporters and their sensitivity to inorganic ions such as Cl^-.

Experimental Section

Materials: Enantiomerically pure compounds M = **1**–**5**, in their flattened-cone conformations, were synthesized and purified by established procedures.[22] Enantiomerically pure $A_{(S)}$ and $A_{(R)}$ hydrochlorides ($AH^+\cdot Cl^-$) were purchased from a commercial source and used without further purification. The same source provided the (*R*)-(−)- ($B_{(R)}$) and (*S*)-(+)-2-butylamine ($B_{(S)}$), which were degassed in the vacuum manifold with several freeze-thaw cycles. The free amphetamines A—that is, either $A_{(S)}$ or $A_{(R)}$ amines—were obtained by treatment of the corresponding hydrochloride enantiomer with aqueous $NaHCO_3$ (1 N).

FT-ICR experiments: The experiments were carried out as described elsewhere.[11–15] In particular, they were performed at room temperature in an APEX 47e FT-ICR mass spectrometer fitted with an ESI source (Bruker Spectrospin) and a resonance cell ("infinity cell") located between the poles of a superconducting magnet (4.7 T). Stock CH_3OH solutions of M = **1**–**5** (1×10^{-5} M), each containing a fivefold excess of the appropriate enantiomer of the free amphetamine (A) or of its hydrochloride ($AH^+\cdot Cl^-$), were electrosprayed through a heated capillary (130 °C) into the external source of the FT-ICR mass spectrometer. The resulting ions were transferred into the resonance cell by use of a system of potentials and lenses and were quenched by collisions with methane pulsed into the cell through a magnetic valve. ESI of M/A methanolic solutions leads to the formation of abundant signals, corresponding to the natural isotopomers of the proton-bound complex $[M\cdot H\cdot A]^+$. The same complexes are formed from ESI of M/$AH^+\cdot Cl^-$ methanolic solutions, together with appreciable amounts of the higher-order proton-bound $[M\cdot H\cdot(A)_2\cdot HCl]^+$ aggregates. Both complexes were monitored and isolated by broad-band ejection of the accompanying ions. Either the $[M\cdot H\cdot A]^+$ family or the $[M\cdot H\cdot(A)_2\cdot HCl]^+$ one were allowed to react with the chiral amine B present in the cell at a fixed pressure, the value of which ranged from 2.3×10^{-8} to 1.1×10^{-7} mbar depending upon its reactivity.

Docking and molecular dynamics calculations: All the computational calculations were carried out and visualized on Intel Linux PCs incorporating Pentium IV CPUs. The Maestro GUI was used as an interface to the software MacroModel 8.6 and 9.0.[23] Molecular Mechanics (MM) calculations (docking) and Molecular Dynamics (MD) simulations were performed with use of the AMBER* force field as implemented in MacroModel. No cutoff was applied for the nonbonded interactions, and the calculations were performed in the gas phase, with selection of the constant dielectric treatment (dielectric constant $\varepsilon = 1.0$). RESP partial atomic charges,[24] for use in the docking and MD simulations, were obtained by use of the Amber molecular dynamics package,[25] starting from ESP charges, obtained from quantum mechanics calculations performed with Gaussian03 software.[26]

ESP charges of the protonated amido[4]resorcinarene $[\mathbf{1}_{(S)}\cdot H]^+$[11–15] were calculated by fitting of ab initio HF/6–31G* molecular electrostatic potential on portions of the molecule (the resorcarene nucleus and the protonated and the nonprotonated chains, shown in Figure 10), optimized at a 6–31G* level, while in the case of the guests A and AH^+, the fitting was done on the entire molecular structure. Before ab initio optimizations, a minimum energy conformation of the host, derived from previous studies,[13] was fragmented and optimized with the semiempirical method AM1. In the case of the guests, the AM1 optimization was instead preceded by a conformational search performed, with the default MacroModel protocol, to locate their corresponding global minimum conformations. The partial atomic charges are specified in the last column of the Cartesian coordinate structures enclosed as Supporting Information (SI; mol2 format).

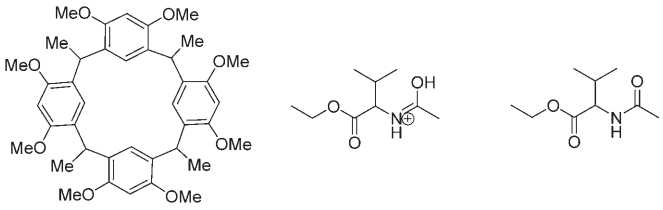

Figure 10. From left to right: fragments (the resorcarene nucleus, the protonated chain and the nonprotonated chain) of the amido[4]resorcinarene $[\mathbf{1}_{(S)}\cdot H]^+$ for which atomic ESP partial charges were calculated by fitting of ab initio HF/6–31G* molecular electrostatic potentials on portions of the molecule.

Insights into the structures and the dynamics of the proton-bound complexes $[\mathbf{1}_{(S)}\cdot H\cdot A]$ and $[\mathbf{1}_{(S)}\cdot H\cdot(A)_2\cdot HCl]^+$ were obtained by recognition simulations, by use of three computational methodologies implemented in MacroModel: that is, the two statistical conformational search procedures—i) Monte Carlo Multiple Minimum (MCMM)[27] and ii) Monte Carlo Multiple Minimum/Low Mode Conformational Search (MCMM/LMCS)[28]—and iii) constant temperature MD runs. In the case of the

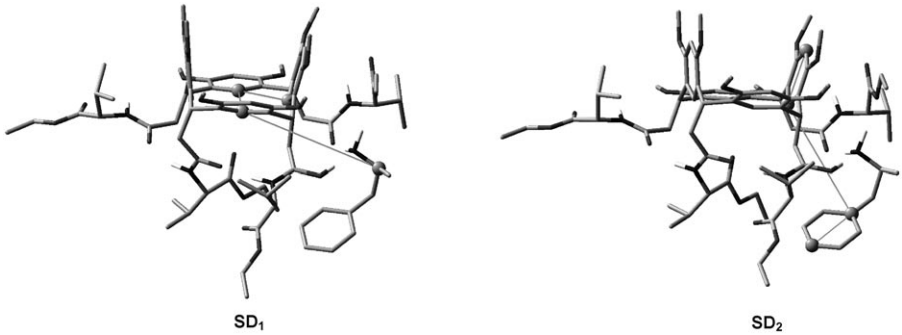

Figure 11. Left: Structural descriptor SD_1, defined to classify the output MCMM/MOLS docking geometries and to graphically depict MD simulations for $[\mathbf{1}_{(S)}\cdot H\cdot A]^+$. Right: Structural descriptor SD_2, defined to classify the output MCMM/MOLS docking geometries and to graphically depict MD simulations for the oscillations of A in *ext*-$[\mathbf{1}_{(S)}\cdot H\cdot A]^+$.

Monte Carlo approaches, the conformational analysis of all the interacting partners was coupled with random rototranslations (MOLS command) of the guest species (A, AH^+, Cl^-, depending on the simulated complex) relative to the $[\mathbf{1}_{(S)}\cdot H]^+$ host kept still in the 3D space (MCMM/MOLS and MCMM/LMCS/MOLS dockings). MCMM/LMCS/MOLS docking was added in this study to the already applied MCMM/MOLS protocol[11–15] so as to increase the probability of producing complete and reasonably homogeneous sampling of the whole potential energy hypersurfaces of our systems. We have indeed already observed that the number of rotatable bonds moved in each docking run (more than 20) was well over the maximum allowed to guarantee exhaustive searches.[14] Each MCMM/MOLS or MCMM/LMCS/MOLS run consisted of 20000 steps. A randomly variable number of rotatable bonds of the pendants of $\mathbf{1}_{(S)}$ and of A, ranging from 2 to $N-1$ (N represents the overall number of variable torsion angles defined in the command file), was subjected to random step variations in the 0°–180° range. With $[\mathbf{1}_{(S)}\cdot H\cdot A]^+$, a total number of 23 torsional degrees of freedom was analysed (the flexibility of the resorcarene skeleton was not directly sampled),[11–15] while with $[\mathbf{1}_{(S)}\cdot H\cdot(A)_2\cdot HCl]^+$, this number increased to 27. The rototranslations of the guest species were limited by the maximum values of 180° for the rotational angle and of 3 Å for the translational movement. In each MCMM/LMCS run, 50% of the steps were LMCS moves. Energy minimizations were performed by the Truncated Newton conjugate gradient (TNCG) procedure and were terminated when the energy gradient root mean square (rms) fell below 0.01 kJ mol^{-1} Å^{-1}. A comparison among the heavy atoms of the output structures was performed in order to eliminate duplicate conformations, 1.0 Å being selected as the maximum allowable separation between pairs of corresponding atoms after superimposition (MULT procedure). All the unique conformers that differed from the global minimum-energy conformation by less than 20 kJ mol^{-1} were saved.

Constant temperature MD simulations with generation of the canonical ensemble were performed at 300 K with a time step of 1.5 fs. The SHAKE algorithm was applied to constrain bonds to hydrogen atoms. Coupling between the temperature bath and the molecules was updated every 0.2 ps. The equilibration period was 50 ps for every run, while the total simulation time was 20 ns. During each trajectory, 5000 structures (frames) were sampled at regular intervals throughout the time course, and were graphically depicted by relating SD to the frame number. Furthermore, all the frames from each MD simulation were fully minimized by the Truncated Newton conjugate gradient (TNCG) procedure until an energy gradient root mean square (rms) below 0.01 kJ mol^{-1} Å^{-1} and incorporated into the corresponding docking output through a further MULT procedure, with the aim of increasing the number of collected geometries. Each recognition simulation (both docking and molecular dynamics) was repeated a few times starting from different arbitrary geometries to produce complete sampling of the whole potential energy hypersurface of the selected $[\mathbf{1}_{(S)}\cdot H\cdot A]^+$ or $[\mathbf{1}_{(S)}\cdot H\cdot(A)_2\cdot HCl]^+$ system. The convergence of the results guarantees the completeness of the study.

The overall conformation of each output docking geometry was classified by the values taken by the ad hoc defined structural descriptors shown in Figure 11 (SD_1 and SD_2).

Acknowledgement

Work was supported by the Ministero dell'Istruzione dell'Università e della Ricerca (MIUR, COFIN), the Consiglio Nazionale delle Ricerche (CNR), and the Istituto Pasteur Fondazione Cenci Bolognetti. B.B. gratefully acknowledges Project "FIRB 2003: RBNE034XSW_005" from the MIUR (Ministero della Università e della Ricerca). The authors express their gratitude to F. Angelelli for technical assistance.

[1] H. Khoshbouei, H. Wang, J. D. Lechleiter, J. A. Javitch, A. Galli, *J. Biol. Chem.* **2003**, *278*, 12070–12077.
[2] D. F. Smith, *CRC Handbook of Stereoisomers: Drugs in Psycopharmacology* (Eds.: D. P. Van Kammen, P. T. Ninan, D. Hommer), CRC Publisher, Roca Baton, FL (USA), **1984**, 297–315.
[3] P. K. Sonsalla, *Drug Alcohol Depend.* **1995**, *37*, 101–105.
[4] K. Kamata, G. V. Rebec, T. Kameyama, *Neurosciences* **1985**, *11*, 105–113.
[5] M. S. Myslobodsky, D. Levin, *Behavioural Brain Research* **1984**, *11*, 145–153.
[6] H. Khoshbouei, N. Sen, B. Guptaroy, L. Johnson, D. Lund, M. E. Gnegy, A. Galli, J. A. Javitch, *PLoS Biol.* **2004**, *2*, 387–393.
[7] S. Povlock, S. G. Amara, *Neurotransmitter Transporters: Structure, Function, and Regulation* (Ed.: M. E. A. Reith), Humana Press, Totowa, New Jersey, **1997**, pp. 1–28.
[8] M. Syringas, F. Janin, B. Giros, J. Costentin, J. C. Bonnet, *Br. J. Pharmacol.* **2001**, *133*, 387.
[9] L. B. Li, M. E. A. Reith, *J. Neurochem.* **2000**, *74*, 1538–1552.
[10] N. Amejdki-Chab, [1]U. A. 1170 du CNRS, U. F. R. de Médecine et Pharmacie, Saint Etienne du Rouvray, France, J. Costentin, [1]U. A. 1170 du CNRS, U. F. R. de Médecine et Pharmacie, Saint Etienne du Rouvray, France, J. J. Bonnet, *J. Neurochem.* **1992**, *58*, 793–800.
[11] B. Botta, M. Botta, A. Filippi, A. Tafi, G. Delle Monache, M. Speranza, *J. Am. Chem. Soc.* **2002**, *124*, 7658–7659.
[12] A. Tafi, B. Botta, M. Botta, G. Delle Monache, A. Filippi, M. Speranza, *Chem. Eur. J.* **2004**, *10*, 4126–4135.
[13] B. Botta, D. Subissati, A. Tafi, G. Delle Monache, A. Filippi, M. Speranza, *Angew. Chem.* **2004**, *116*, 4871–4874; *Angew. Chem. Int. Ed.* **2004**, *43*, 4767–4770.
[14] B. Botta, F. Caporuscio, I. D'Acquarica, G. Delle Monache, D. Subissati, A. Tafi, M. Botta, A. Filippi, M. Speranza, *Chem. Eur. J.* **2006**, *12*, 8096–8105.
[15] B. Botta, F. Caporuscio, D. Subissati, A. Tafi, M. Botta A. Filippi, M. Speranza, *Angew. Chem.* **2006**, *118*, 2783–2786; *Angew. Chem. Int. Ed.* **2006**, *45*, 2717–2720.
[16] C. B. Lebrilla, *Acc. Chem. Res.* **2001**, *34*, 653–661.
[17] J. F. Gal, M. Stone, C. B. Lebrilla, *Int. J. Mass Spectrom.* **2003**, *222*, 259–267.
[18] T. Su, *J. Phys. Chem.* **1988**, *88*, 4102–4103; T. Su, *J. Phys. Chem.* **1988**, *89*, 5355–5356.
[19] The driving force for such different behaviour is illustrated by the MD average structures of $[\mathbf{1}_{(S)}\cdot H\cdot A_{(S)}]^+$ (a) and $[\mathbf{1}_{(S)}\cdot H\cdot A_{(R)}]^+$ (b) obtained by the energy minimization of the structure coordinates derived from averaging of the atomic Cartesian coordinates during the MD run (MDAV MacroModel command). In them, with the H-bond distance between A and the amidocarbonyl moiety of the nearest host pendant kept relatively fixed, both the benzyl and the methyl group of A tend to maximize their van der Waals interactions with the rest of the host structure. This goal is readily achieved by the $A_{(S)}$ guest in the homochiral $[\mathbf{1}_{(S)}\cdot H\cdot A_{(S)}]^+$ adduct a), the methyl group of which (denoted with a grey circle) is always oriented, on average, towards the host pendants, whatever the SD_2 dihedral angle. Contrariwise, the opposite configuration of the $A_{(R)}$ guest in the heterochiral $[\mathbf{1}_{(S)}\cdot H\cdot A_{(R)}]^+$ adduct b) dictates that its methyl group is turned away from the host pendants unless the guest turns

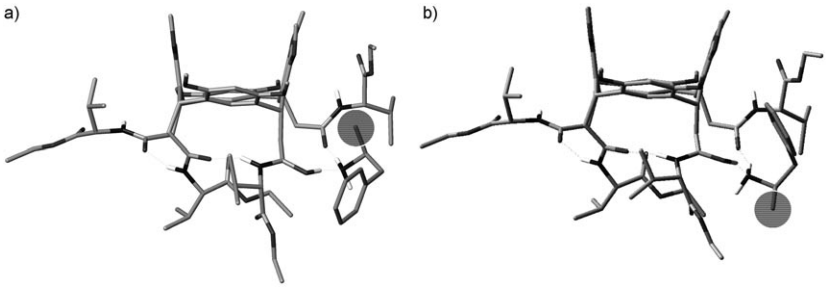

upside down. Only for restricted SD_2 dihedral angles can the methyl group of $A_{(R)}$ establish profitable interactions with the host [see Figure 5 (top) in text, where the maxima at −160, −15 and 160° show completely different intensities with respect to the corresponding peaks at −150, −20 and 150° of Figure 5 (bottom) of text].

[20] M. H. Parker, D. F. Ortwine, P. M. O'Brien, E. A. Lunnery, C. A. Banotai, W. T. Mueller, P. McConnell, C. G. Brouillette, *Bioorg. Med. Chem. Lett.* **2000**, *10*, 2427–2430.

[21] M. Aschi, N. Besker, N. Re, G. Pochetti, C. Coletti, C. Gallina, F. Mazza, *J. Med. Chem.* **2007**, *50*, 211–218.

[22] B. Botta, G. Delle Monache, P. Salvatore, F. Gasparrini, C. Villani, M. Botta, F. Corelli, A. Tafi, E. Gacs-Baitz, A. Santini, C. F. Carvalho, D. Misiti, *J. Org. Chem.* **1997**, *62*, 932–938.

[23] F. Mohamadi, N. G. J. Richards, W. C. Guida, R. Liskamp, M. Lipton, C. Caufield, G. Chang, T. Hendrickson, W. C. Still, *J. Comput. Chem.* **1990**, *11*, 440–467, MacroModel, Schrödinger Inc., Portland, OR 97204, http://www.schrodinger.com.

[24] C. I. Bayly, P. Cieplak, W. D. Cornell, P. A. Kollman, *J. Phys. Chem.* **1993**, *97*, 10269–10280.

[25] http://amber.scripps.edu, University of California, San Francisco, CA (**2004**).

[26] http://www.gaussian.com, Gaussian, Inc., Pittsburgh, PA (**2001**).

[27] G. Chang, W. C. Guida, W. C. Still, *J. Am. Chem. Soc.* **1989**, *111*, 4379–4386.

[28] I. Kolossvàry, W. C. Guida, *J. Comput. Chem.* **1999**, *20*, 1671–1684.

Received: October 5, 2007
Published online: February 22, 2008

